Spatial response framework document

of the HIFI/Herschel Calibration group
C.Kramer
KOSMA, Universität zu Köln
Version 1.8, May, 10th, 2006

Contents

1 Aims and motivation

This paper is a contribution to the joint common framework document of the HIFI calibration group. Its aim is to reach a common understanding and terminology on questions related to the spatial response of HIFI/Herschel, as well as to estimate telescope efficiencies and observing times to obtain those.

While the astronomer is interested in the intensity distribution of an astronomical object in the spatial and frequency domain, all observed intensities are limited by the instrument resolutions. In the spatial domain, the observations are convolved with the antenna diagram, i.e. the point spread function of the telescope. In frequency domain, the observations are smoothed by the spectrometer response function.

Here, I will only talk about the spatial domain.

The internal hot-/cold-calibration translates backend counts into antenna temperatures (see Part I of the framework document by Ossenkopf 2003). There are two principal methods to derive antenna independent temperatures. Either a very accurate system model is needed or observations of celestial calibrators whose brightness temperature distribution is well known. The latter approach is generally used,

- to derive telescope efficiencies, i.e. to do a photometric calibration,
- to measure the half power beamwidths of the main beam,
  and to measure the beam profile, i.e. to map the point spread function.

Measuring the beam profile is important, since Herschel will detect a significant fraction of the total power from outside the main lobe, i.e. from sidelobes. This holds in particular for the highest frequencies. When observing extended sources, any extended errorbeam pickup may become important. To accurately correct for this pickup, it my not be sufficient to apply a constant scale factor, as is often done, since the pickup depends on the source structure in the spatial and frequency domain.

2 Introduction - The antenna diagram

This introduction defines the parameters used to describe the spatial response but it is not specific to the Herschel Space Observatory. This is meant as a coherent, though brief, guidline to the reader but does not intend to replace the relevant literature (e.g. Rohlfs & Wilson 1996, Gordon et al. 1992). The knowledgeable reader may want to skip this chapter.

The directional response of a telescope is described by its antenna diagram or point spread function. Single dish telescopes have one main lobe, which detects most of the incoming power, and sidelobes. In addition, the telescope may detect weak, extended emission from other parts of the forward half sphere and from the back.

The antenna pattern is the telescope response to a point source, as a function of angle, normalized to unity on axis: $P_n(\theta, \phi) = P(\theta, \phi)/P_{\max}$. The beam solid angle Ω_A is defined by

$$\Omega_A = \int\int_{4\pi} P_n(\theta, \phi) d\Omega.$$

Due to diffraction, even a perfectly constructed antenna detects radiation through a main lobe and several sidelobes.

The resolving power of a telescope is characterized first of all by the half power beamwidth (HPBW) of the main lobe. The HPBW scales with the observing wavelength and inversely with the telescope diameter. The HPBW depends in addition on the illumination edge taper.

For a Gaussian beam, i.e. in zeroth order approximation, the beam solid angle is related to the HPBW via: $\Omega_A = \pi \mathrm{HPBW}^2/(4\ln 2) = 1.133\ \mathrm{HPBW}^2$.

2.1 Beam width and edge taper

The half power beamwidth is proportional to the observing wavelength λ divided by the diameter of the telescope D: HPBW$\propto \lambda/D$. The constant depends on the edge taper, i.e. the illumination of the telescope (among other factors like blockage). This is also a diffraction pattern, but the inner part illuminating the telescope is usually well approximated by a Gaussian. Goldsmith (1982) gives an empirical formula relating the HPBW with the edge taper T_E [dB]:

$$\mathrm{HPBW} = 0.8\sqrt{T_E}\frac{1}{\pi}\alpha(T_E)\frac{\lambda}{D}. \quad (1)$$

The truncation of the Gaussian illumination broadens the main beam. This effect is corrected for by $\alpha(T_E)$ which is listed in Table 1 of Goldsmith (1982). He gives values of $\alpha(5\,\mathrm{dB})$=1.89, $\alpha(10\,\mathrm{dB})$=1.42 (i.e. HPBW = $1.2\lambda/D$), $\alpha(15\,\mathrm{dB})$=1.24, $\alpha(20\,\mathrm{dB})$=1.13.

Strong tapering leads to an enlarged beam size since the primary is not "fully used". But it also leads to low sidelobes. A low edge taper on the other hand decreases the HPBW but diffraction then causes the sidelobes and spillover to rise. This leads to a reduction of the efficiency with which the telescope detects power through its main beam. It is thus clear that a compromise has to be found for the edge taper which leads to a good resolving power and at the same time to reduced sidelobe levels and thus high efficiency (e.g. Rohlfs & Wilson 1996, pp.125).

2.2 Source flux densities

2.2.1 General case

In general, the flux density per beam is the convolution of the antenna diagram with the source brightness distribution.

The **flux density** $S_{\nu,tot}$, that is the power radiated per unit area and per unit frequency from a radio source at a given frequency, is given by

$$S_{\nu,tot} = \int_{\Omega_S} B_\nu(T_B)\psi(\theta,\phi)d\Omega = \frac{2k\nu^2}{c^2}\int_{\Omega_S} J_\nu(T_B)\psi(\theta,\phi)d\Omega. \quad (2)$$

ψ describes the normalized spatial brightness distribution of the source: $\psi(0,0) = 1$ and $\psi(\theta,\phi)$=0 outside the source. Ω_S is the source solid angle: $\int_{4\pi}\psi(\theta,\phi)d\Omega$. T_B is the Planck brightness temperature of the source. $J_\nu(T_B)$ is the Rayleigh-Jeans brightness temperature at the frequency ν: $J_\nu(T_B) \equiv T_{RJ} = \frac{h\nu}{k}[\exp(\frac{h\nu}{kT_B}) - 1]^{-1}$, where λ is the wavelength of observation and k is the Boltzman constant.

2.2.2 Circular disk of uniform temperature

For a source with uniform temperature and the shape of a disk of diameter θ_s the flux density equals

$$S_{\nu,tot} = \frac{2k\nu^2}{c^2}\frac{\pi}{4}\theta_s^2 J_\nu(T_B). \quad (3)$$

This assumes that the uniform temperature translates directly into a uniform brightness temperature, i.e. we neglect limb darkening.

3 The antenna temperature

3.1 The aperture efficiency

The aperture efficiency describes the efficiency to detect point sources. It is defined as the ratio of effective antenna area $A_{\rm eff}$ and geometrical area of the aperture $A_{\rm geom}$

$$\eta_A = \frac{A_{\rm eff}}{A_{\rm geom}} \tag{4}$$

with the geometrical area of the aperture $A_{\rm geom} = \pi(D_{\rm teles}/2)^2$ and the effective area $A_{\rm eff}$, which in turn is defined via

$$\lambda^2 = A_{\rm eff}\Omega_A \tag{5}$$

(e.g. Kraus 1984).

3.2 The forward efficiency

This is the ratio of power detected from the forward hemisphere to the total power detected, i.e.

$$\eta_l = \frac{\Omega_{2\pi}}{\Omega_A} \tag{6}$$

with $\Omega_{2\pi} = \int_{2\pi} P_n(\theta,\phi)d\Omega$.

At ground based telescopes, skydips are usually used to derive this efficiency. In orbit, this method does not work. A new method is therefore proposed in Part I of the framework document (Ossenkopf 2003).

3.3 The measured antenna temperature

The measured antenna temperature is is given by the convolution integral of antenna diagram and source brightness distribution:

$$T_A^*(\theta,\phi) = \frac{1}{\eta_l\Omega_A}\int_{source} P(\theta-\theta',\phi-\phi')J_\nu(T_B)\psi(\theta',\phi')d\Omega' \tag{7}$$

The detected brightness temperatures are expressed in antenna temperatures, as usual in radio astronomy. Throughout this document, I will use antenna temperatures on the T_A^* scale. It relates to the T_A' scale via $T_A' = T_A^*\eta_l$ with the forward efficiency η_l as defined above.

Equation 2 simplifies to $S_{\nu,tot} = (2k/\lambda^2)J_\nu(T_B)\Omega_S$. Together with equation 5 we can then write

$$\begin{aligned} T_A^*(\theta,\phi) &= \frac{1}{\eta_l}\frac{S_{\nu,tot}A_{\rm eff}}{2k}\frac{1}{\Omega_S}\int_{source} P(\theta-\theta',\phi-\phi')\psi(\theta',\phi')d\Omega' \\ &= \frac{1}{\eta_l}\frac{S_{\nu,tot}A_{\rm eff}}{2k}\frac{\Omega_{\rm sum}}{\Omega_S} = \frac{1}{\eta_l}\frac{S_{\nu,tot}A_{\rm eff}}{2k}K = \frac{1}{\eta_l}\frac{S_{\nu,beam}A_{\rm eff}}{2k} \end{aligned} \tag{8}$$

with the beam weighted source solid angle $\Omega_{\rm sum} = \int_{source} P(\theta-\theta',\phi-\phi')\psi(\theta',\phi')d\Omega'$ and the correction factor $K = \Omega_{\rm sum}/\Omega_S$ (Baars 1973) which equals 1 for pointlike sources (and exact pointing!). It is calculated in section 4.3 for a Gaussian beam. The **flux density per beam** $S_{\nu,beam}$ used in Table 5 is defined as $S_{\nu,tot}\times K$.

4 Telescope efficiencies

Both, aperture and beam efficiency, describe the relative telescope efficiency in detecting source radiation. Efficiencies range between 0 and 1 and thus they do not depend on the telescope diameter.

4.1 Aperture efficiency and point source sensitivity

The aperture efficiency can be determined via the observed peak antenna temperature T_A^* of a pointlike source when its total flux density $S_{\nu,tot}$ is known. From Eqs.(6),(8), we find

$$\eta_A = \frac{A_{\rm eff}}{A_{\rm geom}} \;\text{ and }\; \frac{\eta_A}{\eta_l} = \frac{2k}{A_{\rm geom}} \frac{T_A^*}{S_{\nu,tot} K} \equiv \frac{2k}{A_{\rm geom}} \frac{1}{\chi_{\rm PSS}} \tag{9}$$

thereby also defining the point source sensitivity in Jansky per Kelvin which is often used instead of the aperture efficiency: $\chi_{\rm PSS} = S_{\nu,beam}/T_A^*$. Both measures reflect the overall phase errors (due to e.g.bad focus or surface errors), spillover, blockage, optical losses.

4.2 Main beam efficiency

The main beam efficiency is defined as the percentage of power entering through the main beam between the first nulls

$$\eta_{\rm mb} = \frac{\Omega_{\rm mb}}{\Omega_A} \;\text{ and }\; \frac{\eta_{\rm mb}}{\eta_l} = \frac{\Omega_{\rm mb}}{\Omega_{2\pi}} \tag{10}$$

with $\Omega_{\rm mb} = \int_{\rm mb} P_n(\theta,\phi) d\Omega$.

Circular disk of uniform temperature filling the beam. From the above equation and the equations (3,5,8), for a disk shaped source completely filling the main beam ($\Omega_{\rm sum} = \Omega_{\rm mb}$) we find, without assumptions about the beam shape:

$$\frac{\eta_{\rm mb}}{\eta_l} = \frac{T_A^*}{J_\nu(T_B)} \tag{11}$$

This equation also gives a recipe on how to measure the main beam efficiency.

The antenna diagram of a real telescope shows sidelobes and maybe error patterns. Measuring sources which are larger than the beam size and using eq. (11) will thus lead to an effective beam efficiency $\eta'_{\rm mb}$, or source coupling efficiency, varying with the size of the source. See below for a fomula to correct for the influence of the source size (Eq. 16, however assuming a Gaussian beam.). See e.g. Gordon et al. (1992, p.340) for a discussion of the implications for the observer. Figure 1 shows the variation of the effective efficiency with source diameter for the IRAM 30m telescope (Greve et al. 1998). The effective efficiency stays almost constant for sources larger than the HPBW by upto a factor of about 3.

4.3 Simplifications assuming a Gaussian beam shape

First order corrections for non-pointlike sources: the correction factor K. For a Gaussian beam with HPBW θ_b:

$$P(\theta) = \exp[-\ln 2 (2\theta/\theta_b)^2]$$

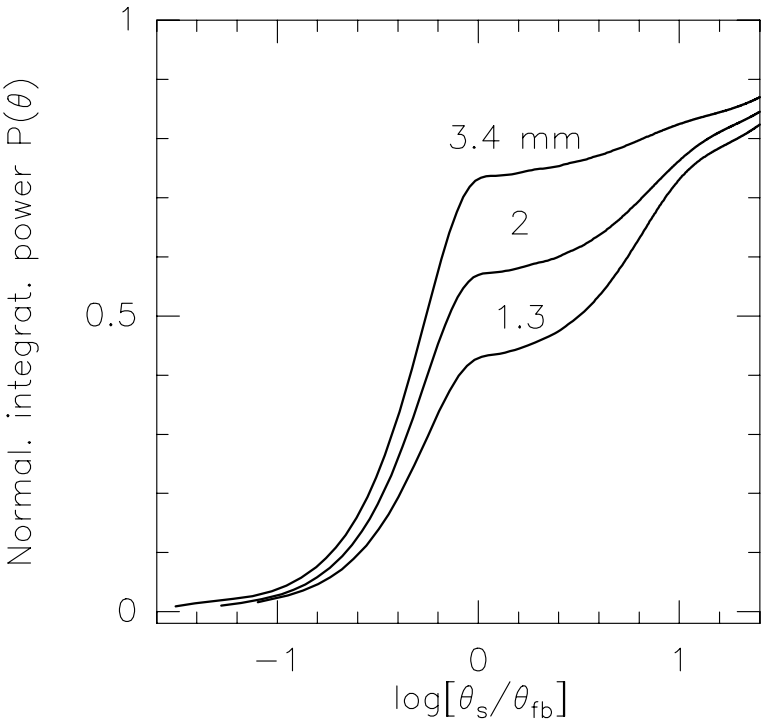

Figure 1: The source coupling efficiency at the IRAM 30m telescope (Greve et al. 1998). The relative power $P(\Omega)$ received in the solid angle Ω of opening θ_s is given as fraction of the full width to first minimum θ_{fb} ($\theta_{fb} \approx 2.4\,\mathrm{HPBW}$). $P(\Omega) \approx \eta_{\mathrm{mb}}$ at $\log[\theta_s/\theta_{fb}] = 0$.

centered on a uniform source disk

$$\psi(\theta) = \begin{cases} 1 & \text{for } \theta \le \theta_{\mathrm{s}}/2 \\ 0 & \text{else} \end{cases}$$

the integral eq. (7) can be rewritten:

$$T_A^*(\theta = 0) = \frac{1}{\eta_l}\frac{1}{\Omega_A} 2\pi J_\nu(T_B) \int_0^{\theta_s/2} \exp\Big[-\ln 2(2\theta/\theta_b)^2\Big]\theta d\theta.$$

(Here we used the approximation $\sin\theta = \theta$.) The integration results in:

$$T_A^*(\theta = 0) = \frac{1}{\eta_l}\frac{\Omega_{\mathrm{mb}}}{\Omega_A} J_\nu(T_B)\Big[1 - \exp(-x^2)\Big] \quad \text{with} \quad x = \sqrt{\ln 2}\ \ \theta_s/\theta_b. \tag{12}$$

For a Gaussian beam we find:

$$\Omega_{\mathrm{mb}} = \int_{mb} P(\theta)\theta d\theta = \frac{1}{4\ln 2}\pi\theta_b^2 \approx 1.133\,\theta_b^2. \tag{13}$$

For a Gaussian beam, Ω_{mb} equals Ω_A and $\Omega_{2\pi}$, and $\eta_l = 1$, $\eta_{\mathrm{mb}} = 1$.
Eqs. (2, 5, 12) then lead to a formula for the correction factor K:

$$T_{\mathrm{A}}^* = \frac{1}{\eta_l}\frac{S_{\nu,tot}A_{\mathrm{eff}}}{2k}K \quad \text{with} \quad K = \frac{1 - \exp(-x^2)}{x^2} \le 1. \tag{14}$$

valid for a Gaussian beam with HPBW θ_b and a disklike source of diameter θ_s.

The factor K corrects for the reduction in antenna temperature when observing a source which has a non-negligible diameter compared to the half power beam width. It equals 1 for

a point-source. For $\theta_s/\theta_b = 0.5$ the correction K equals 0.92. For $\theta_s/\theta_b = 1$ the correction K equals 0.72.

Beam efficiency. Though the beam efficiency formally equals 1 for a Gaussian beam, a real telescope beam will always consist of sidelobes lowering the beam efficiency. In addition, a circular source of known brightness temperature exactly filling the main beam, is usually not available.

Using eq. (12), we find:

$$T_{\rm A}^* = \frac{\eta_{\rm mb}}{\eta_l} T_{\rm mb} \qquad \text{with} \qquad T_{\rm mb} = J_\nu(T_B)\Big[1 - \exp\Big[-\ln 2\Big(\frac{\theta_s}{\theta_b}\Big)^2\Big]\Big]. \tag{15}$$

The main beam efficiency can be estimated from the measured antenna temperature of a planet of known brightness temperature and diameter:

$$\eta_{\rm mb} = \frac{\eta_l T_{\rm A}^*}{T_{\rm mb}} = \frac{\eta_l T_{\rm A}^*}{J_\nu(T_B)\Big[1 - \exp(-x^2)\Big]} \qquad \text{with} \qquad x = \sqrt{\ln 2}\ \ \theta_s/\theta_b. \tag{16}$$

For an extended source ($\theta_s \geq 2.6\theta_b$) and a clean Gaussian beam (that is a source completely filling the beam: $\Omega_{\rm sum} = \Omega_{\rm mb}$) we thus find to a good accuracy $T_{\rm mb} = J_\nu(T_B)$, and again

$$\frac{\eta_{\rm mb}}{\eta_l} = \frac{T_{\rm A}^*}{J_\nu(T_B)}. \tag{17}$$

Note that the factor $(1 - \exp(-x^2)^{-1}$ in eq. (16) is smaller than 1.01 for a source which fills the 20dB width of a Gaussian beam, i.e. which is a factor 2.58 larger than the HPBW ($\theta_{-20dB} = 2.58\ \theta_b$).

Relating main beam and aperture efficiencies. The aperture and the main beam efficiency are related via the beamwidth when assuming a Gaussian beam. Equations 14 and 16 lead to:

$$\frac{\eta_{\rm mb}}{\eta_l} = \frac{\eta_{\rm A}}{\eta_l}\frac{A_{\rm geom}\Omega_{\rm mb}}{\lambda^2} = \frac{\eta_{\rm A}}{\eta_l}\frac{A_{\rm geom}}{\lambda^2}\frac{\pi}{4\ln 2}\theta_b^2 \tag{18}$$

It follows from equation 1 that

$$\eta_{\rm mb} = \eta_{\rm A} T_E \alpha(T_E)^2 \frac{0.8^2}{16\ln 2} = \eta_{\rm A} A(T_E). \tag{19}$$

The aperture efficiency is proportional to the beam efficiency. The constant A depends only on the edge taper and is independent of the frequency. For an edge taper of 11 dB, as expected for the HIFI mixers, $A \sim 1.28$.

4.4 Imperfections

The antenna diagram of a telescope obviously depends on blockage by e.g. a subreflector, on radiation spilling over the edge of the primary dish, on surface deviations, etc.. Some of these effects are unavoidable. It is important to know their impact on the beam pattern. The beam pattern will for instance turn out to be not any longer completely axial symmetric.

4.4.1 Blockage

On-axis radio telescopes suffer from blockage by the subreflector and its support legs. Blockage reduces the effective area of the telescope and thus obviously leads to a reduction of efficiencies.

Depending on the temperature of the blocking material, blockage may lead to an increase of the system temperature. Also, ambient radiation may be scattered into the beam by the blockage contributing to the $(1-\eta_l)$ part. Blockage may also lead to standing wave problems due to reflections. As a result, the aperture efficiency is reduced.

4.4.2 Spillover

There are several contributions to spillover: Radiation diffracted at the edge of subreflector may enter the feed horn directly (forward spillover). Likewise, radiation of the background may be diffracted at the edge of the main dish and thus reach the subreflector and then enter the feed horn (backward losses) contributing to the $(1-\eta_l)$ part and to the extended pattern. Spillover is to some extend unavoidable and depends largely on the edge-taper.

4.4.3 Surface deviations

Deformations of mirror surfaces from their ideal shape lead to perturbations of the wavefront and thus to a degradation of the beam shape. Usually, the largest mirror, i.e. the primary, is prone to have the largest deviations from its, in our case, parabolic shape. The Ruze-formula gives the resultant decrease of efficiencies for small-scale uncorrelated surface errors:

$$\eta_A = \eta_{A0} \times \exp\Big(-\Big(\frac{4\pi\sigma_s}{\lambda}\Big)^2\Big) \tag{20}$$

In general, large-scale deformations distort the central part of the beam, while intermediate-scale deformations produce one, or several, underlying, extended error-beams. This is e.g. documented for the IRAM 30m telescope (Greve et al. 1998).

4.4.4 Alignment errors

Optical errors like defocus, coma, and astigmatism may stem from misaligned mirrors, for instance a misaligned subreflector or a misaligned receiver. These errors degrade the wavefront and thus the beam shape. The wavefront deformations can be described by combinations of low-order Zernike polynomials.

4.5 Radiometer formula

To estimate the integration time needed, I use the radiometer formula and the assumptions listed in Table 4:

$$T_{A,rms}^{*,SSB} = \frac{T_{sys}^{SSB}}{\sqrt{0.25\,\Delta\nu\,t_{\rm on+off}}}. \tag{21}$$

The integration time $t_{\rm on+off}$ given in Table 5 is thus solely the `on+off` time of e.g. double-beamswitched observations. I assume here perfect white noise, i.e. no degradations of the noise temperatures due to drifts, no standing waves, etc.. $\Delta\nu$ is the channel (fluctuation) band width of the spectrometer.

5 Optical design of the Herschel Telescope

The Herschel Telescope is an axi-symmetric 3.5 m diameter Cassegrain telescope consisting of a parabolic primary (M1) and hyperbolic secondary (M2). There is no mechanism for refocussing once the telescope is in orbit. The operating wavelength range is 80 μm to 670 μm. A few important parameters are listed in Table 1. The illumination of the secondary is planned to be about **11 dB edge taper** (N.Whyborn, priv. comm.). The secondary is undersized relative to the primary. The effective diameter of the primary is thus only **3.28 m**. This value was used for all estimates of the beam widths and efficiencies described below.

The present design of the support structure for the Herschel subreflector (M2-mirror) consists of 6 legs which are pairwise placed at about half radius of the primary M1 mirror. The subreflector itself is placed inside a hexapod structure. With this design, blockage will occur both when radiation from sky enters the primary, as also when the radiation is reflected to the subreflector. The design is similar to that of the JCMT.

The **total purely geometrical obscuration ratio** is about 7.7% and is specified to be be less than **8%** (Astrium, 05/04/02). See Table 1.

Table 1: Geometrical parameters of the Herschel telescope. Column 3 gives the purely geometrical blockage relative to the effective aperture. The total geometrical blockage is the sum of M1 central hole (2.9%), 3 Hexapod holes (0.5%), shadow of hexapod legs + M2 barrel (1.7%), shadow of hexapod legs (path from secondary to primary) (2.5%). The effective blockage will be still larger than the total geometrical blockage.

	diameter	geometrical blockage
Primary:	3.5 m	
Effective aperture	3.28 m	
Secondary:	308.1 mm	0.9%
Central hole in primary:	560 mm	3%
Total blockage		7.7%

6 Estimate of aperture and main beam efficiencies

6.1 Blockage

Telescope efficiencies are reduced due to blockage. In case of central blockage, this effect is enhanced by the edge taper. The strong obscuration in the dish center of Herschel will thus cause a stronger than 8% effective obscuration. See Harris (1988) for discussions and calculations on the influence of blockage and edge taper.

Table 2 lists estimated main beam efficiencies for the Herschel telescope showing the effect of blockages.

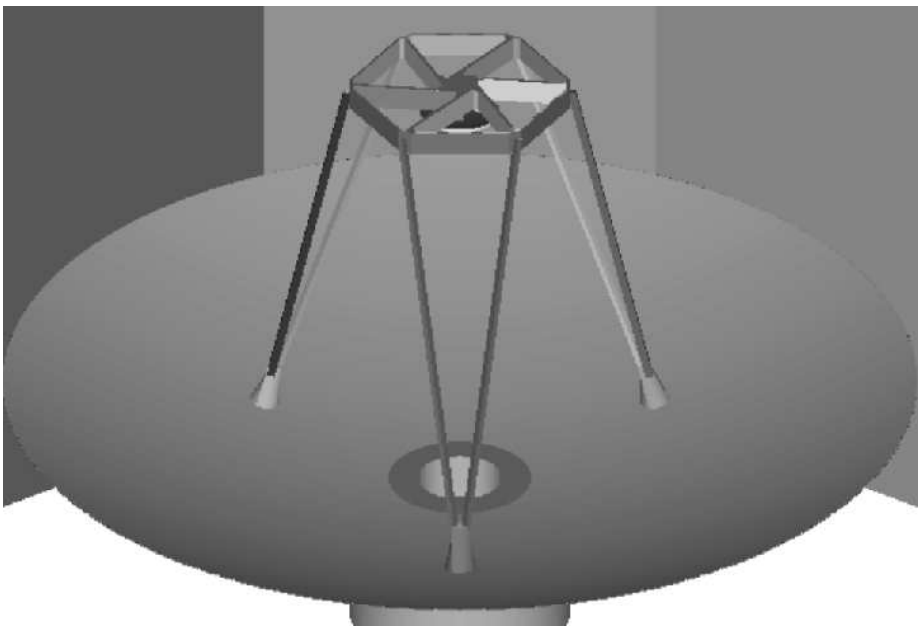

Figure 2: The Herschel primary, secondary, and its support structure (taken from Astrium 2002).

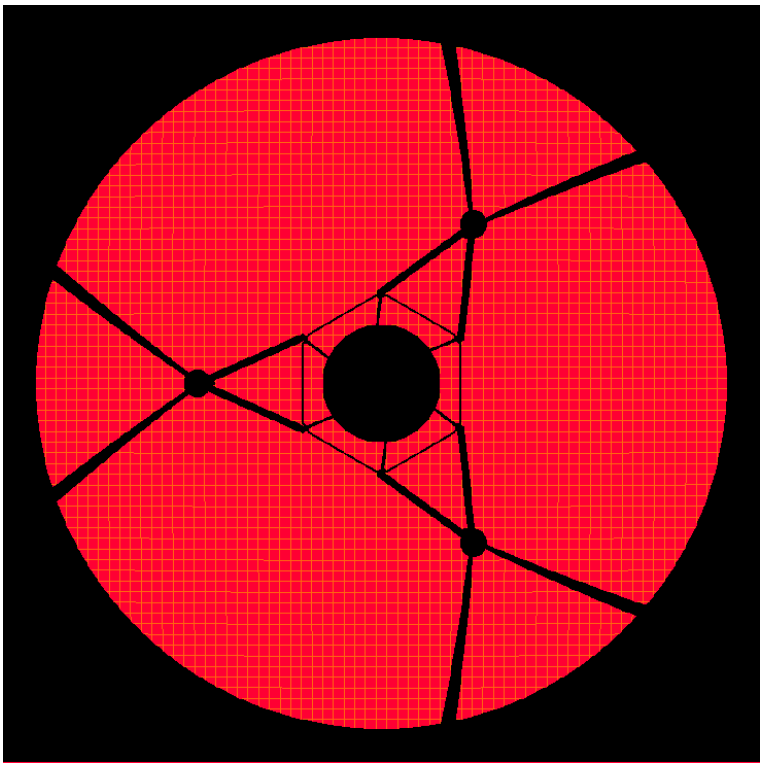

Figure 3: Central obscuration at FOV center due to projection of hexapod, secondary, and secondary frame onto the primary (current baseline concept with rectangular legs cross section and large scatter cone, from Daniel.de.Chambure@esa.int and D.Beintema, 15.Jan.2003).

Figure 5 shows the calculated beam pattern at 900 GHz for the full blockage. The efficiencies and sidelobe levels for a perfect surface do not depend on the frequency as is shown in Fig. 6.

The computations start from the following simplifying assumptions: The amplitude distribution in the aperture is assumed to be Gaussian and with 11dB edge taper in our case. The

Table 2: Calculated aperture η_{A0} for a perfect surface and main beam efficiencies η_{mb} for Herschel for the effective aperture of **3.28 m**, an edge taper of **11 dB**. These efficiencies are frequency independent. Calculations are based on one-dimensional and two-dimensional diffraction programs of Urs Graf (KOSMA). The 1D-calculation assumes radial symmetry and uses only the central blockage by the M1 hole. The 2D-calculation uses the full illumination pattern shown in Fig. 3.

	η_{A0}	η_{mb}	calculation
No blockage	82%	90%	1D
Only blockage by secondary	80%	85%	1D
Only blockage by central hole	76%	76%	1D
Full blockage (cf.Fig.3)	71%	72%	2D

phase distribution is assumed here to be flat, i.e. surface errors are not considered. The transformation between amplitude+phase distribution in the aperture to the beam pattern (PSF) is simply given by a Fourier transform (Fraunhofer diffraction), in the limiting case of far-field. Since we want to know the far field PSF, the calculation is easy, in principle. (Another way of thinking of that transformation is in terms of Huygens elementary waves.) The results of this calculation are shown in Table 2 and Figures 7 and 5. The expected aperture efficiency is $\eta_{\rm A0} = 71\%$.

6.2 Detailed modelling of the beam shape

In reality, the amplitude aperture distribution may not be perfectly Gaussian and not perfectly centered on the primariy and secondary mirrors. These deviations from the ideal case can be calculated from the HIFI horns for the two polarisations and the six bands, and the size and position of the mirrors of the focal plane unit. Such calculations of the diffraction are conducted by Tully Peacocke and his group and will eventually lead to an improved prediction of the HIFI antenna diagrams.

6.3 Surface errors

Another possible source of reduction of telescope efficiencies are deviations of the primary (and other mirrors) from their perfect shape, i.e. surface errors. The overall wavefront error of the primary is specified to be less than 6 μm (Astrium, 05/04/02). Main contributors are the reflectors polishing specifications (3.4 μm) and the cool down distortions (1.5 μm). The surface error is half the wavefront error. The **total surface error** is thus specified to be less than 3 μ**m rms**. This leads to a reduction of the aperture efficiency, most notable in band 6. At 1.9 THz, the aperture efficiency is reduced by $\sim 4\%$, from the frequency independent value of a perfect surface of 71% to about 67% (Fig. 7). This estimate uses the Ruze-Formula (see Introduction) and thus assumes small scale errors.

Large scale errors are not expected. The primary is made from 12 separate panels which are "welded" together during construction. We are not supposed to see the difference from a monolithic mirror.

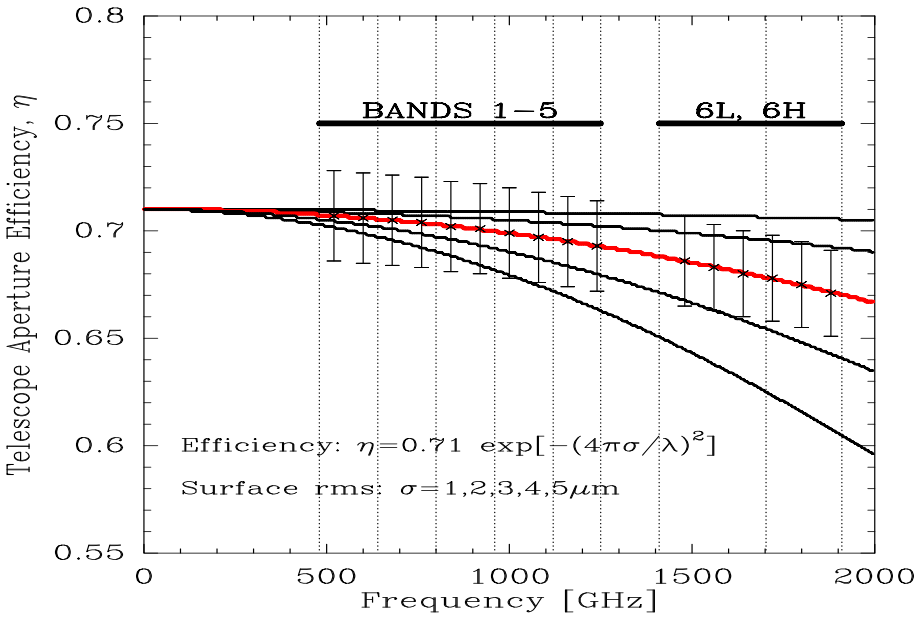

Figure 4: Predicted aperture efficiencies assuming an aperture efficiency at long wavelengths of 0.71, as predicted by the 2-dimensional diffraction modelling (Table 2). The Ruze formula (Eq. 20) is used to estimate the frequency dependence for five different surface errors. Crosses mark predicted efficiencies at 16 frequencies covering the HIFI mixer bands in steps of 80 GHz for a surface rms error of 3 μm. Errorbars show the scatter expected for a 3% calibration accuracy. Variations of the illumination by the 14 mixers of the 7 bands may lead to jumps at the band edges.

6.4 Optical losses

Yet another source of degradation are optical losses of the mirror surfaces specified in the "Herschel Telescope Specification" (SCI-PT-RS-04671). These contribute to the $(1 - \eta_l)$ part, but are at present ignored in the following discussion.

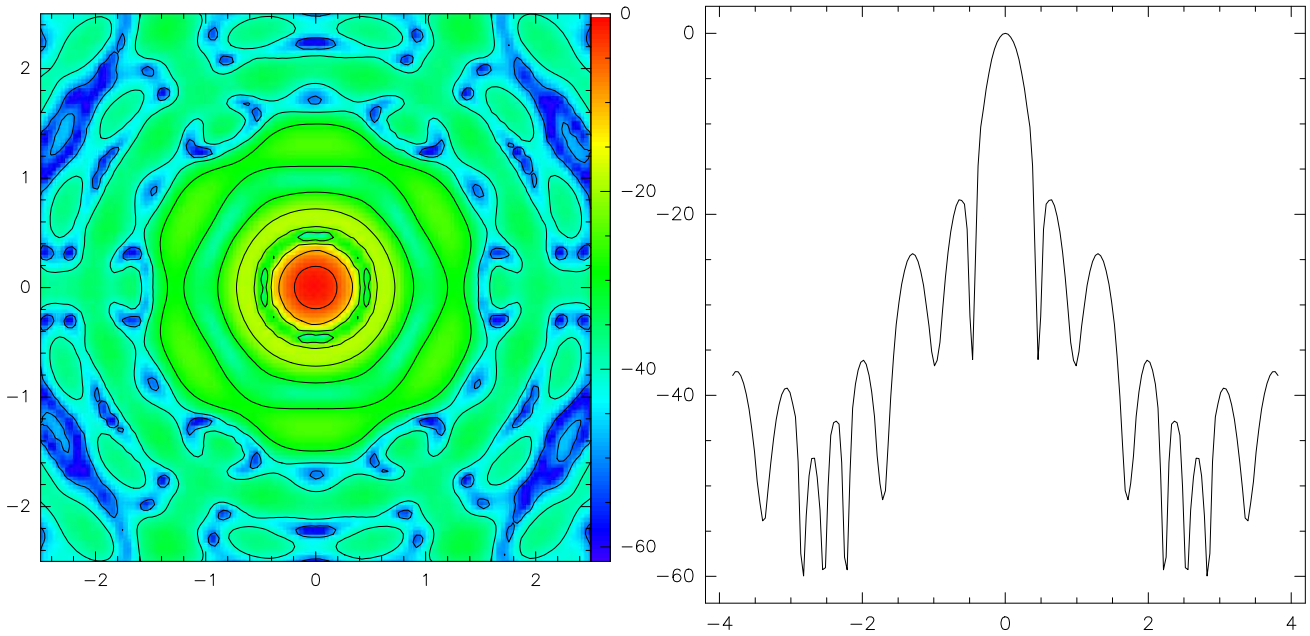

Figure 5: **Left.** Two-dimensional beam pattern derived from the full blockage shown in Fig. 3 under the assumption of an edge taper of 11 dB. The calculation was done at 900 GHz. Units of x- and y-axis are arcminutes. Contourlevels are −3dB and −10dB, in steps of −10dB. The diffractions pattern of the hexapod legs is visible at −30dB. **Right.** Cut for $y = 0$. The units of the x-axis is arcminutes, the units of the y-axis is dB. The first sidelobes are above −20dB.

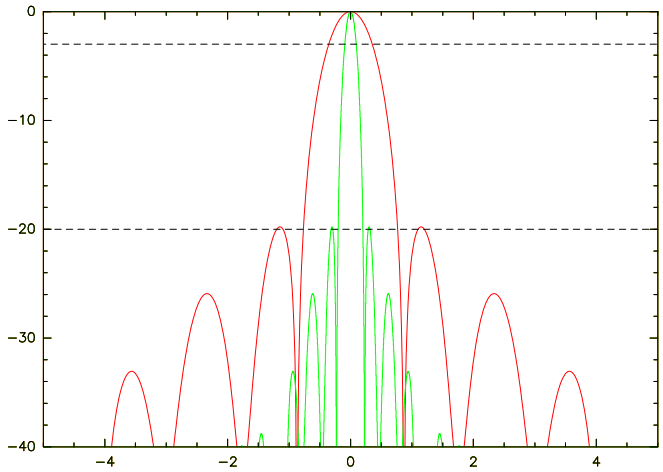

Figure 6: Cut through two antenna diagrams at 1900GHz and 500GHz. This is based on a one-dimensional calculation, i.e. assuming radial symmetry and taking into account the blockage due to the central hole. See Table 6. Sidelobe levels stay constant with frequency.

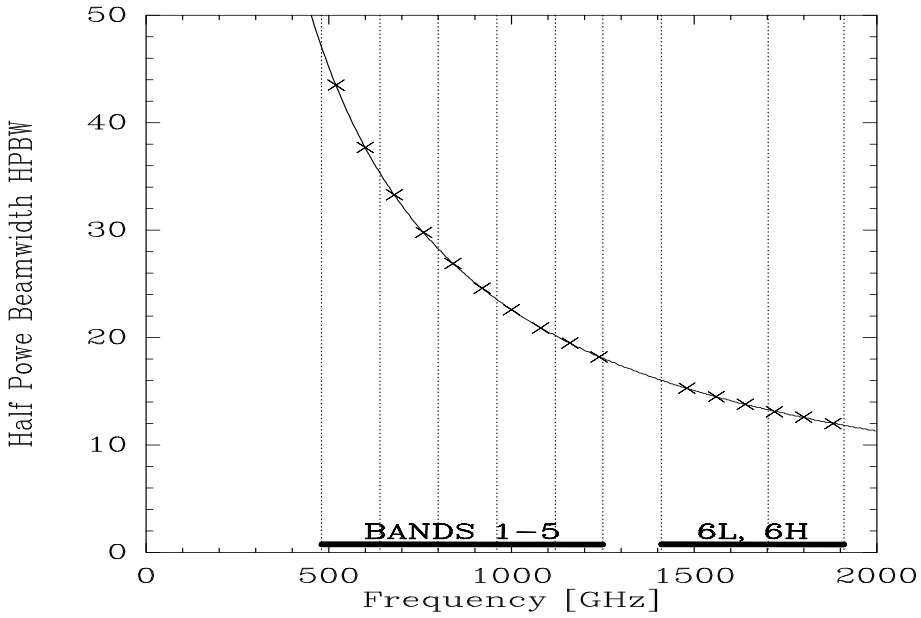

Figure 7: Predicted half power beamwidths for HIFI/Herschel (Eq. 1) assuming an edge taper of $-11\,\mathrm{dB}$ and $\alpha(T_E) = 1.42$. In case the illumination varies between individual mixers, the curve may show show jumps at the band edges.

Table 3: Predicted aperture efficiencies and half power beamwidths (cf. above Figures) at 16 frequencies, spaced by 80 GHz, in bands 1–5 and bands 6L & 6H, for a surface error of $3\,\mu$m rms and a calibration uncertainty of 3%.

Frequency GHz (1)	η_A % (2)	$\Delta\eta_\mathrm{A}$ % (3)	HPBW $''$ (4)
520.00	70.7	2.1	43.5
600.00	70.6	2.1	37.7
680.00	70.5	2.1	33.3
760.00	70.4	2.1	29.8
840.00	70.2	2.1	26.9
920.00	70.1	2.1	24.6
1000.00	69.9	2.1	22.6
1080.00	69.7	2.1	20.9
1160.00	69.5	2.1	19.5
1240.00	69.3	2.1	18.2
1480.00	68.6	2.1	15.3
1560.00	68.3	2.0	14.5
1640.00	68.0	2.0	13.8
1720.00	67.8	2.0	13.1
1800.00	67.5	2.0	12.6
1880.00	67.1	2.0	12.0

7 Continuum observations of solar system bodies

7.1 Time estimate

Celestial objects are needed as calibrators in order to derive the telescope efficiencies, the HPBW, and the beam shape in general. The aim here is to estimate the observing times needed to use solar system bodies as calibrators.

The HIFI document "Solar system bodies as calibration sources" by Herpin, Gerin, and Kramer (2003) describes the selection and currently available models of planets and asteroids. Uranus, Mars, Saturn, and Ceres are possible candidates.

Here, I use the current estimates of their brightness temperatures to estimate the resulting antenna temperatures when observed with HIFI/Herschel. Table 4 lists the basic assumptions for the calculation and Table 5 lists the resulting estimated antenna temperatures, signal-to-noise ratios, and observing times. The formulae used are described and listed in the Introduction.

For a DSB mixer with no sideband rejection and a planetary continuum signal entering twice, i.e. through both sidebands, the point source sensitivity has to be divided by ~ 2: $T_A^*(\mathrm{SSB}) = 2 \times T_A^*(\mathrm{DSB})$. The antenna temperature of a continuum source of known brightness temperature is then:

$$T_A^*(\mathrm{SSB}) = \frac{S_{\nu,beam}}{\chi_{\mathrm{PSS}}} \times 2. \tag{22}$$

To ease comparison with spectroscopic observations, all antenna temperatures are on the SSB scale in this document. (The single-sideband gain ratio equals 0.5 only in first assumption!)

Table 4: Assumptions for the time estimates. The bandwidth in col.**(2)** is only 100 MHz, although the total bandwidth of HIFI for bands 1–5 is 4 GHz, and 2.4 GHz for band 6 (see chapter 7.4). Column **(3)**: For the system temperatures, I used the baseline values for total power, single polarisation, optics and telescope losses included (Whyborn 2001). The newer value for band 6 is used here, as presented in Leiden (Dec. 2002). Column **(4)**: For the aperture efficiencies, I use the values derived above. The point source sensitivity $\chi_{\mathrm{PSS}} = 2k/A_{\mathrm{geom}} \times \eta_l/\eta_A$ (col.**(5)**) is given by the aperture efficiency (see Eq. 9). For the forward efficiency, I assume $\eta_l = 1$. For the HPBWs **(6)**, Eq. 1 was used assuming an edge taper of 11 dB, and $\alpha(T_E) = 1.42$ (Goldsmith 1982).
Column **(7)** lists the rms antenna temperatures reached after 1 sec of total integration time.

Frequency	Bandwidth $\Delta\nu$	System temperature T_{sys}^{SSB}	Aperture efficiency η_A	Point source sensitivity χ_{PSS}	HPBW	$T_{A,rms}^{*,\mathrm{SSB}}$ $(t_{int} = 1\,\mathrm{sec})$
[THz]	[GHz]	[K]		[Jy/K]	[″]	[mK]
(1)	(2)	(3)	(4)	(5)	(6)	(7)
1.90	0.1	2000.	0.67	488.	12.	400.
0.50	0.1	180.	0.71	460.	45.	36.

For the calculation, I used dates for which the sources are visible (Table 8). The Martian diameter is strongly varying. I selected two dates for which Mars is rather small and rather large.

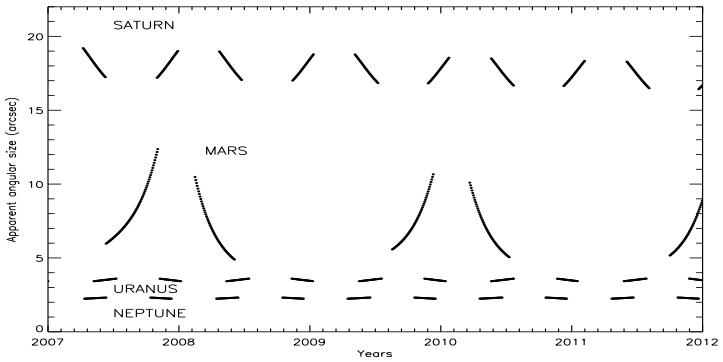

Figure 8: Visibility of planets for Herschel between 2007 and 2012 (by D.Teyssier).

7.2 Choice of solar system bodies

It is important to have a list of primary calibrators at hand for Herschel/HIFI since none of the planetary bodies is visible all the time. The range of allowed sun elongation angles (angle between the telescope pointing and the sun) is limited to $90 \pm 30°$ (IID-A). Thus, any planet inside the Earth orbit, including the Moon, cannot be observed with Herschel. This also means that the visibility of Mars, Uranus, and the other outer planets is restricted: any given planet is observable only during two times every year or so, every 2 years for Mars (Fig. 8).

These restrictions call to prepare for several primary calibrators - one is clearly not sufficient. Secondly, the calibrators serve different calibration purposes. A strong emitter like Mars is suited to map the antenna diagram. However, Mars is a complicated object with its solid surface and thus it may be difficult to model its brightness temperature distribution with the required accuracy (Herpin et al. 2003). Therefore, Uranus appears to be better suited as primary calibrator to derive telescope efficiencies.

In Table 5, I give time estimates to observe Mars, Uranus, Saturn, and Ceres. **The brightness temperatures used here need to be adapted when new, more accurate and reliable planetary model results become available.**

Mars. For Mars, an average temperature of 215 K $\langle T_B \rangle$ at the mean distance to the sun $\langle R \rangle$ of 1.5237 AU (Astronomical Almanac 1989 E43) is assumed. The planetary temperature varies with distance R (Ulich 1981):

$$T_B = \langle T_B \rangle \times \sqrt{\frac{\langle R \rangle}{R}}. \tag{23}$$

The Mars diameter varies strongly between $\sim 4''$ and $\sim 15''$. Due to the visibility constraints of Herschel, the variation during observations will be restricted to about $5''$ and $12''$ (Fig. 8).

Uranus. For Uranus, the model of R.Moreno (1998) predicts a brightness temperature of 60 K at 1.9 THz. For the lower frequency, the empirical function of Griffin & Orton (1993) is used.

Saturn. For Saturn, the values of Hildenbrand et al. (1985) are used.

Ceres. For Ceres, we use the value measured by Altenhoff et al. (1996) at 250 GHz, thus assuming that it is a black body. See Müller & Lagerros (1998, 2002) for a comparison of asteroid models in the wavelength range 5μm to 200μm and ISOPHOT observations.

Table 5: Time estimate for observations of solar system bodies with HIFI/Herschel. Column (3) gives the planetary diameter at the time of observation (col.2). Column (4) gives the observing frequency. Column (5) is the brightness temperature used for the calculation of total fluxes given in (6). Fluxes per beam are listed in (7) and used to derive the antenna temperature expected with HIFI in column (8): this is simply given by total flux per beam, $S_{\nu,beam}$, divided by the point source sensitivity. Column (9) gives the corresponding signal-to-noise ratio after 1 sec of on+off integration time. Beware that all overheads are neglected here! Columns (10) and (11) give the integration times needed to achieve signal-to-noise ratios of 20 dB and 30 dB respectively.

Body	Date	D	ν	T_B	$S_{\nu,tot}$	$S_{\nu,beam}$	T_A^*(SSB)	SNR	t_{int}^{20dB}	t_{int}^{30dB}
		[″]	[THz]	[K]	[Jy]	[Jy]	[K]	1 sec	[sec]	[sec]
(1)	(2)	(3)	(4)	(5)	(6)	(7)	(8)	(9)	(10)	(11)
Saturn	15/ 5/2007	16.9	1.90	135.0	55495.	29788.	122.15	305.	107msec	11sec
Mars	1/10/2007	9.7	1.90	225.8	35251.	28245.	115.82	290.	119msec	12sec
Mars	1/ 7/2007	6.3	1.90	222.0	14726.	13370.	54.83	137.	1sec	53sec
Uranus	1/ 7/2007	3.6	1.90	60.0	660.	640.	2.62	7.	4min	6h
Ceres	1/ 1/2008	0.6	1.90	169.0	94.	94.	0.38	1.	180min	300h
Saturn	15/ 5/2007	16.9	0.50	131.4	4870.	4640.	20.16	560.	32msec	3sec
Mars	1/10/2007	9.7	0.50	225.8	2851.	2806.	12.19	339.	87msec	9sec
Mars	1/ 7/2007	6.3	0.50	222.0	1194.	1186.	5.15	143.	488msec	49sec
Uranus	1/ 7/2007	3.6	0.50	77.0	117.	117.	0.51	14.	50sec	83min
Ceres	1/ 1/2008	0.6	0.50	169.0	8.	8.	0.03	1.	178min	296h

7.3 Discussion of the time estimate

Saturn and Mars are bright sources (Tab. 5) and allow to measure the telescope efficiencies with a high signal-to-noise ratio at all frequencies. In the worst case, it takes only 1 sec to achieve a 20dB signal-to-noise ratio on Mars at 1.9 THz when it is only 6.4″ in size. For Uranus, it needs 4 minutes of on+off integration time at the same frequency to achieve the same SNR. Though Ceres is very small in angular diameter, its black body temperature is warmer than that of Uranus and Saturn. Only one second of observing time is needed to accomplish a SNR of 1 (i.e. 0 dB). However, it would take excessive time to construct a beam map using Ceres. Even with the large and rather bright Saturn, it takes 12 sec to reach a SNR of 30dB.

Aperture efficiency: Ideally, a point source is needed to derive aperture efficiencies. Mars' diameter varies between 4 and 15″ and is thus pointlike even at 1.9 THz for part of the time. It is much stronger than Uranus. But it is only visible part of the time. And modelling is difficult.

Uranus is pointlike, weak, but modelling is probably easier.

Ceres appears to be suited as well. It is pointlike. It is only a factor of 2 weaker than Uranus when in opposition. When Ceres is suited to measure the aperture efficiency, then several of the larger asteroids may be suited as well!

A good pointing accuracy is needed, especially for these observations. The specified accuracy is 3.5″, i.e. a third of the beam width at 1.9 THz only. Peaking up may thus be necessary before measuring the aperture efficiency.

Note that the aperture efficiency, i.e. the point source sensitivity, drops by 6% when the pointing is offset by 0.25 HPBW. It drops by 22% when the pointing is offset by 0.5 HPBW. In general, the efficiency drops by a factor $\exp(-f^2)$ when the pointing is offset by f HPBW.

Beam efficiency: Ideally, sources filling the main beam are needed to measure the main beam efficiency. With the Herschel beams between 40 and 10″, Saturn and Mars appear to be

suited. The choice depends on visibility and the availability of planetary models.

7.4 The best observing mode

The Allan stability time shifts to smaller times with increasing channel width since the radiometric white noise contribution is then decreasing. Schieder & Kramer (2001) give an analytic formula:

$$T'_{\rm Allan} = T_{\rm Allan}(B/B')^{1/(\beta+1)} \tag{24}$$

where B is the (fluctuation) channel width and β is the slope of the drift noise contribution which may vary between 1 and 2. [1]

Current estimates of the system stability of HIFI/Herschel indicate that 100 MHz is the maximum binning width when chopping at maximum speed, i.e. at 3.5 Hz (due to HEMT IF-amplifiers, see note of N. Whyborn of 6/2/03 and related documents). Cf. Table 4.

7.4.1 Pointed observations and small maps of the PSF

The Total Power (position switched) or On-the-Fly modes have much longer cycle times for on+off observations which involve slewing times and are therefore not suitable for the continuum observations discussed here. We therefore plan to use the **double-beamswitch mode (DBS)**.

7.4.2 Large maps of the PSF

Self chopping effects due to the restricted chopper throw of $3'$ at most has to be taken into account when conducting extended maps in beam switched (BS) mode. For such maps, a combination of BS with the OTF-mode may be the best choice. To estimate the influence of standing waves on the continuum data, off source integrations in BS-mode may be needed. Note also, that the chop orientation is fixed to the observatory orientation.

In table 6 we estimate the observing time needed to map the point spread function. The size is defined by the sidelobes (cf. Fig. 6).

Table 6: Estimate of on-source integration times for maps.

frequency	grid	20dB	30dB	
500 GHz	$20''$	1 sec	3 sec	(time per position on Saturn)
		$3' \times 3'$	$5' \times 5'$	(map size)
		2 min	6 min	(total on time)
1900 GHz	$5''$	1 sec	12 sec	(time per position on Saturn)
		$1' \times 1'$	$2' \times 2'$	(map size)
		3 min	36 min	(total on time)

[1] Recent tests of the behaviour of drift noise using large band widths indicate negative values of β rendering the definition of the Allan minimum time useless. This result still needs to be validated (V.Ossenkopf, priv. commun., April 03).

7.5 Observing strategy

7.5.1 Efficiencies

1. Measuring the aperture efficiency by pointed observations of a source with small angular diameter relative to the beam, will immediately allow to judge the optical quality of the telescope system. In the best case, the observations will be consistent with the expectations from the models.

2. Two perpendicular scans of the same source will reveal the half power beamwidths. These scans can be relatively short in spatial length and done in the standard double beam switch mode.

3. Another check are pointed observations of more extended sources, ideally filling the main beam, in order to measure the main beam efficiency.

4. The derived aperture and main beam efficiencies will be compared with each other to check their consistencies. In the approximation of a poorly Gaussian beam, these two efficiencies are directly related via the half power beamwidth (see eq. 18).

5. The above observations need to be conducted at least for each mixer of HIFI, since illumination (edge taper) and alignment accuracy may vary.

6. If none of these measurements reveal any deviations from our expectations, the sidelobe and errorbeam pattern of the point spread function are probably well behaved and need not be checked in all details.

7.5.2 Sidelobes

To measure the extended sidelobes of Herschel, the source ideally needs to be pointlike and very strong. But its absolute flux does not need to be known! Sidelobes may be very narrow. Thus, accurate pointing is again of great importance.

The map sizes needed to detect sidelobes at a given level, are estimated in Table 6. Maps are larger than the chopper throw of $3'$ at the low frequencies (bands 1 and 2) when low sidelobe levels need to be detected.

In Table 5, I estimate the time needed to measure the extended errorbeams below 20dB, disregarding all overheads.

7.6 Open questions

- A use case for extended on-the-fly beamswitched maps needs to be written. Also, a precedure to re-construct the beam maps from the self-chopped data is yet missing.

- To what extend do standing waves alter the above time estimates and conclusions?

- PACS observations of the point spread function, especially at shorter wavelengths (down to 60μm), should be very helpful in judging the optical quality of the telescope. The different tapering of the secondary has -of course- be taken into account when comparing with the PSF seen by HIFI. Also, PACS is not diffraction limited at short wavelengths.

8 Literature

1. Astrium, Straylight, Powerpoint presentation, 12/06/02
2. Astrium, Herschel Telescope Optical Design Justification, 8/04/02 HER.NT.183.T.ASTR
3. Astrium, Optical design analysis, 02/04/02 HER.NT.0026.T.ASTR
4. Chambure ESTEC, SCI-PT/08865, 17-April-2001
5. Bensch F., Stutzki J., Heithausen A. 2001, A&A, 365, 285
   Methods and constraints for the correction of the error beam pick-up in single dish radio observations
6. Downes D. 1988, **Radio Astronomy Techniques**
   In: Appenzeller I., Habing H.J., Lena P. (eds.), Evolution of Galaxies Astronomical Observations, Lecutre Notes in Physics 333. Springer Verlag, Berlin-Heidelberg, p. 351
7. Gordon M.A. et al. 1992, A&A, 264, 337
   Observations of radio lines from unresolved sources: telescope coupling, Doppler effects, and cosmological corrections
8. Goldsmith P.F. 1982, **Quasi-Optical Techniques at Millimeter and Submillimeter Wavelengths**, In: Button, K.J. (ed.), Infrared and Millimeter Waves, Vol. 6: Systems and Components, Academic Press, New York, pp. 277-343
9. Greve A., Kramer C., Wild W., 1998, A&A, 133, 271
   The beam pattern of the IRAM 30m telescope
10. Harris A., 1988, International Journal of Infrared and Millimeter Waves (ISSN 0195-9271), 9, 231
    Telescope illumination and beam measurements for submillimeter astronomy
11. Herpin F., Gerin M., Kramer C., 2003 (Internal HIFI report, L3AB/HIFI/CAL/2003-01)
    Solar system bodies as calibration sources
12. Kutner M.L., Ulich B.L. 1981, ApJ, 250, 341
    Recommendations for calibration of millimeter-wavelength spectral line data
13. Moreno R. 1998, Ph.D. thesis, Observatoire de Paris-Meudon
    Observations milimetrique et submillimetrique des planetes geantes. Etudes de Jupiter apres la chute de la comete SL9
14. Müller T.G., Lagerros J.S.V. 2002, A&A, 381, 339
    Asteroids as calibration standards in the thermal infrared for space observatories
15. Ossenkopf 2003
    Part I of the HIFI/Herschel framework document: Intensity calibration
16. Schieder R., Kramer C. 2001, A&A, 373, 746
    About the use of Allan variance measurements
17. Whyborn N.D. 1997, FIRSU Conference
    The HIFI Heterodyne Instrument for FIRST: Capabilities and Performances

18. Whyborn N.D. 2001, HIFI Science Preparatory Workshop, Leiden, 16-19th December 2001
HIFI Sensitivity and Time Estimator

9 Changes

- Change to v1.8:
  - Updated Table 4 and 5 to reflect a surface error of 3mu.

- Change to v1.7:
  - Added equation 19
  - Corrected some confusion between 3 and 6μm surface errors. I now assume consistently a surface error of 3μm in Sec.6.1, Fig.4, Table 3.
  - Corrected factor 2 error in Eq 18 after discussion with R.Moreno
  - Added comment on drop of the point source sensitivity, i.e. aperture efficiency, for different pointing errors (see Sec.7.3)

- Change to v1.5:
  - Added plot of expected half power beamwidths
  - Added plot of expected main beam efficiencies
  - Added table of expected values

- Change to v1.4:
  - RID no.4 resulting from the calibration review: cross check aperture and main beam efficiency where possible (RID = review item discrepancies)
  Reaction: Revised chapter on the "Observing strategy". Reference to equation 18.
  - Small changes to the chapters on "Best observing mode" and "Open questions".

- Change from v1.2 to v1.3:
  - Improvement of time estimate of beam maps

- Change from v1.1 to v1.2:
  - Small changes after suggestions from David Teyssier and Volker Ossenkopf

- Change from v0.3 to v1.0:
  - Moved appendix to introduction, elaborating on formulae, SSB/DSB issue
  - Detailed listing of assumptions going into the time estimate.
  - Taken into account comments from Nick Whyborn, Volker Ossenkopf, Maryvonne Gerin, Urs Graf
  - The wavefront error is specified to be less than 6″.

- Change from v0.2 to v0.3:
  - Three documents merged
  - All standard formula moved to Appendices
  - DSB temperatures changed to single side band temperatures
  - time estimate: effective diameter changed from 270cm to 328cm
  - time estimate for 480 GHz added